Materials and Design 180 (2019) 107892

Contents lists available at ScienceDirect

Materials and Design

journal homepage: www.elsevier.com/locate/matdes

Micro fracture investigations of white etching layers

Ashish Kumar Saxena [a], Ankit Kumar [a,b], Michael Herbig [a], Steffen Brinckmann [a], Gerhard Dehm [a], Christoph Kirchlechner [a,*]

[a] Max-Planck-Institut für Eisenforschung GmbH, Max-Planck-Straße 1, 40237 Düsseldorf, Germany
[b] Delft University of Technology, Department of Materials Science and Engineering, Mekelweg 2, 2628CD Delft, the Netherlands

HIGHLIGHTS

- The fracture toughness of WELs and comparable microstructures were obtained using elasto-plastic micro fracture experiments
- The fracture toughness of WELs is comparable to martensite
- The fracture toughness of WELs can be estimated from the hardness via a proposed empirical relation.
- Various criteria for interpreting the J-integral at small scales are quantitatively compared and discussed.
- We determined critical defect size in WELs.

GRAPHICAL ABSTRACT

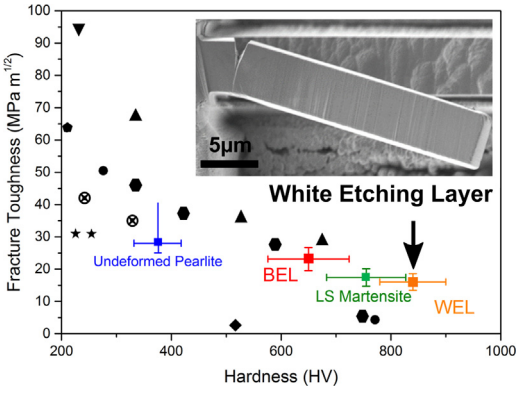

ARTICLE INFO

Article history:
Received 27 February 2019
Received in revised form 17 May 2019
Accepted 27 May 2019
Available online 29 May 2019

Keywords:
Rail steel
White etching layer
Elasto plastic fracture mechanics
Micro cantilever testing

ABSTRACT

The fracture behavior of a white etching layer formed on the rail surface in pearlitic steels during the rail-wheel contact is investigated using indentation-based microcantilever fracture tests. The sample thickness is in the order of 5 µm. The local fracture toughness of the white etching layer, its neighboring brown etching layer, martensite and pearlite with similar chemical composition are determined and compared to ferritic steels. All samples show stable crack growth accompanied by significant plasticity at the crack tip. The toughnesses scale inversely with the microhardness. The white etching layer exhibits a toughness of 16.0 ± 1.2 MPa m$^{1/2}$ which is in the same range as the fully martensitic steel. It is shown that the local fracture toughness can be roughly estimated based on the Vickers hardness of the white etching layer. Also, an estimation of a critical defect size in white etching layers which considerably furthers the understanding of crack initiation is made in this study. Furthermore, various criteria for analyzing the elasto plastic fracture toughness are compared.

1. Introduction

White Etching Layers (WELs) are nano-crystalline regions in iron carbon based alloys which were subjected to a complex loading scenario comprised of (i) severe mechanical loading, (ii) thermal loading and, often, (iii) electrical loading. WELs are of enormous economic importance as they cause degradation of materials subjected to contact fatigue failure [1–6]. Examples are rail tracks and wheels [1,6] or hard-turned surfaces [7]. The origin of WELs and their forming mechanisms are currently discussed intensively [2,8–13]. The two most prominent formation models either hypothesize the formation via a martensitic

* Corresponding author.
E-mail address: kirchlechner@mpie.de (C. Kirchlechner).

https://doi.org/10.1016/j.matdes.2019.107892

transformation of the pearlitic steel [4,14,15] or the formation via severe plastic deformation [16,17].

WELs are acting often as crack initiation sites [1,2,4–6,18,19]. Two crack types are reported: (i) cracks perpendicular to the WEL surface propagating through the WEL and (ii) cracks at the interface between WEL and pearlite [18,20,21]. Perpendicular cracks initiate at the sample surface and propagate rapidly through the WEL until they reach the interface [21]. This behavior has been associated with the mechanical properties of WELs which are commonly assumed to be brittle. However, up to now only indentation has been performed to assess the mechanical properties of WELs which only gives access to hardness values, but the fracture toughness remains unknown. At the WEL-pearlite interface, the cracks either are deflected and run along the interface or propagate straight through the pearlite. The interface cracks can also start at the sample surface and propagate along the WEL-pearlite interface. These crack often form branches at a later stage [21]. Even though numerous studies on crack initiation and propagation in WEL exist, a thorough understanding of the WEL formation mechanisms and of the crack formation in the WEL vicinity is currently missing.

New views on the microscopic behavior of materials are offered by the ability to isolate micron and submicron sized material volumes using focused ion beam (FIB) machining followed by mechanical testing of these samples. This comprises methods for measuring the material strength during compression, tension and bending [22–24], and local measurements of the fracture toughness [25]. *In situ* micromechanical fracture testing is well established for brittle materials (e.g. single crystal Si [26], bulk metallic glasses [27] and hard coatings [28–30]) in which linear elastic fracture mechanics (LEFM) applies. However, for semi-brittle/ductile materials – in which significant plasticity occurs before failure – elasto-plastic fracture mechanics (EPFM) are required. EPFM is less established at the micron scale and still no thorough standardization exists. For testing semi-brittle materials at the micrometer scale, EPFM gained elevated attention recently. One example is the fracture properties of tungsten [31–34]. But also other material systems like NiAl [35], metallic glass thin films [27], severely deformed pearlitic wires [36,37] were tested recently by applying EPFM at the micrometer scale.

The aim of this work is to study the fracture toughness of WELs in order to pave the way for a thorough understanding of crack initiation and nucleation in rail-wheel contacts. For this purpose, we are using FIB milled pre-notched micro cantilevers. The fracture toughness of WELs is measured and compared to brown etching layers (BELs), lab simulated martensite and undeformed pearlitic steel. All materials have identical chemical composition and only differ by their microstructure.

2. Experimental procedure

2.1. Material selection

The specimens were obtained from a curved rail track with a radii of 400 m. The rail track has a total load passage of approximately 33 megatons/year for a period of 3 years in-service. The initial material was a pearlitic rail steel (grade R350HT) with a composition of Fe-0.72C-1.1Mn-0.56Si-0.11Cr (in wt%). In the as-delivered state, the material exhibited a fully pearlitic microstructure with a colony size of 20 μm and an interlamellar spacing of 150 nm. Patches of WEL were present close to the contact surface and these patches have a different microstructure than the base material. Microstructure details of the WEL are reported by Kumar et al. [38]. The rail was cut using a diamond wire saw into 5 $\times$ 4 $\times$ 2 mm^3 sized samples (further denoted as macro-sample) and subsequently mechanically polished with 4000 grit paper and etched with 2% Nital solution. The polished surface was perpendicular to the train running direction. Finally, the microstructure was investigated using light optical microscopy and scanning electron microscopy (SEM). This revealed the size and distribution of the WEL, a transition region (called brown etching layer (BEL)) and the undeformed pearlite.

Apart from the macro-samples extracted from the in-service rail, two lab simulated martensite macro-samples were prepared from the same steel composition. The lab simulated material was processed in a Gleeble 1500 thermo-mechanical-simulator at 200 °C/s heating rate, heated until 730 °C (A3 temperature), immediately followed by rapid quenching with a cooling rate of 400 °C/s to room temperature in helium atmosphere. This procedure resulted in a fully martensitic microstructure.

2.2. Micro cantilever preparation

The micro fracture cantilevers were milled with a FIB on three macro-samples, all containing WEL, BEL and undeformed pearlite regions. The single cantilever geometry was used to measure the fracture toughness [26,31]. The samples had a rectangular cross-section with the intended crack plane defined by the train running direction and the rail surface normal. The ratios of cantilever length (L):height (W):width (B) of each milled cantilever were nominally 5:1:1, while the lengths of the cantilevers were in between 20 and 25 μm (Fig. 1a).

For FIB milling, a Zeiss Auriga® dual beam microscope equipped with a Nano Patterning and Visualization Engine (NPVE) was operated with 30 keV Ga^+ ions. The milling currents were gradually reduced from a coarse milling step with 16 nA and a dose of 60 nC/μm^2 (16 nA||60 nC/μm^2), via an intermediate step at 2 nA||40 nC/μm^2 and fine milling at 600pA||40 nC/μm^2. Straight through-thickness notches

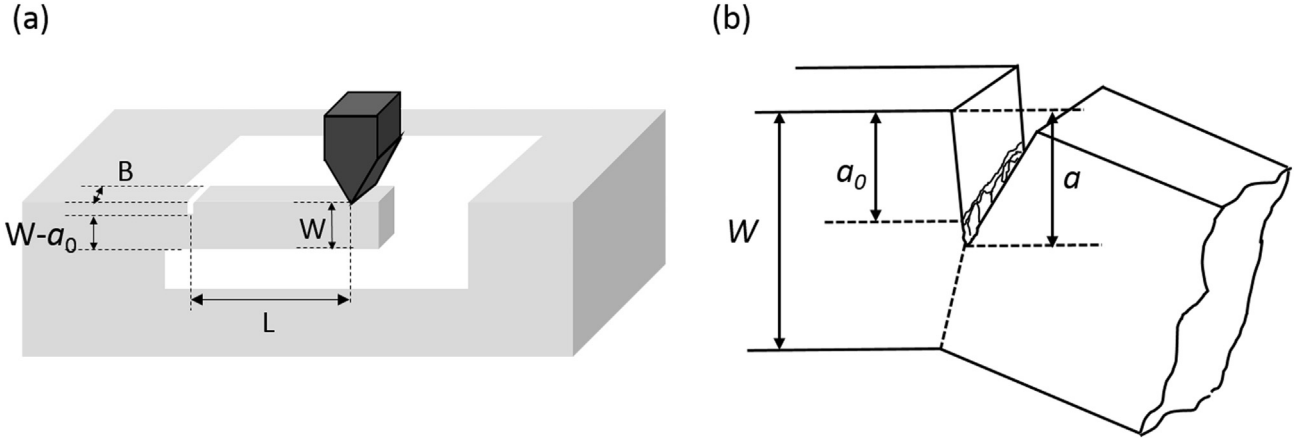

Fig. 1. (a) Schematic of the geometry of the micro-cantilevers prepared by FIB milling. (b) Definition of the crack length.

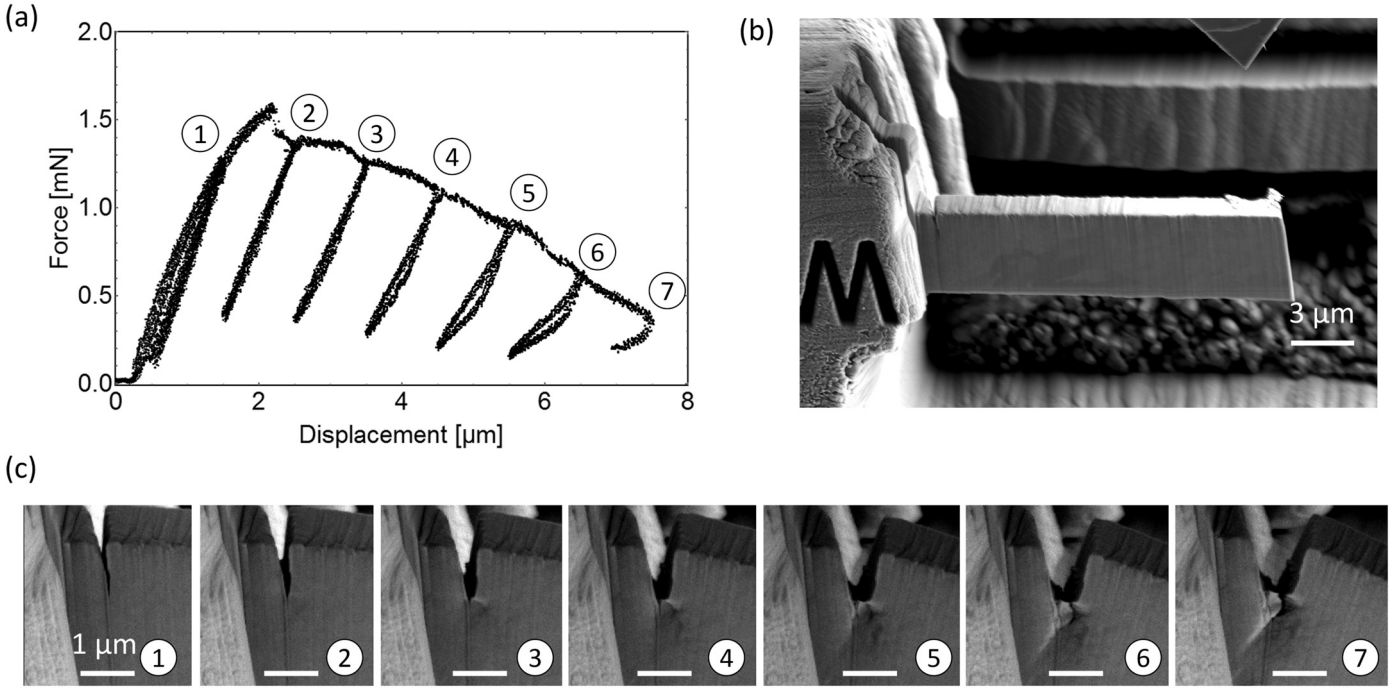

Fig. 2. (a) Representative force-displacement curve of a white etching layer (WEL) sample. The curve shows the initial elastic and later significantly plastic deformation and fracture. (b) Secondary electron SEM image of the tested white etching layer micro cantilever. (c) Sequential elasto-plastic crack propagation recorded by *in situ* SEM with positions highlighted in the force-displacement curve (a).

were made with 10pA||60 nC/μm^2 and resulted in a final notch depth of about 1.0 μm. Finally, the side surfaces were re-polished to guarantee a constant pre-notch depth and to avoid side-notch effects. It has to be noted that special precautions – like the successive reduction of milling currents and times as well as the choice of significantly large FIB free space in the vicinity of the cantilever – were taken to avoid material re-deposition at the back and lower cantilever surface, as re-deposition would have affected the obtained fracture toughness considerably.

The initial notch length (a_0) was measured from high resolution SEM micrographs recorded in a Gemini 500 field emission SEM. The a/W ratio was in the range of 0.2–0.3 (see Fig. 1b). To ensure sufficient statistics, at least 4 data sets for each microstructure (i.e. WEL, BEL, lab simulated martensite and undeformed pearlite) were tested.

2.3. Fracture experiment

The micro-cantilever fracture experiments were performed *in situ* in a Zeiss Gemini 500 SEM equipped with an ASMEC Unat II nanoindenter (ASMEC GmbH, Radeberg, Germany). A conductive diamond wedge indenter with an opening angle of 60° and a wedge length of 10 μm was used to load the cantilevers under displacement control. The loading rate was constant at 20 nm/s. The force-displacement curves and *in situ* videos of bending/fracture were recorded for all beams. Numerous loading-unloading cycles were used to determine the crack propagation via the unloading stiffness, as previously proposed by Wurster et al. [31].

2.4. Analysis of the fracture toughness

For the determination of the fracture toughness (J_c), we are following the approach by Wurster et al. [31], who separated the elastic and plastic contributions to the J integral (Eq. (1))

$$J = J_{elastic} + J_{plastic} \tag{1}$$

$J^{(i)}_{elastic}$ is calculated from LEFM (Eq. (2)), where $K^{(i)}_{IQ}$ represents the plane strain stress intensity factor as calculated from Eq. (3):

$$J^{(i)}_{elastic} = \left(K^{(i)}_{IQ}\right)^2 \frac{\left(1-\nu^2\right)}{E}, \tag{2}$$

$$K^{(i)}_{IQ} = \frac{F^{(i)}_Q L}{B W^{3/2}} f\left({}^{a^{(i)}}/_{w}\right), \tag{3}$$

where ν is the Possion's ratio, E is the elastic modulus, $F^{(i)}_Q$ is the acting force at a time increment i. The geometry parameters are defined in Fig. 1. The dimensionless geometric factor $f({}^{a}/_{W})$ for rectangular cantilevers (Eq. (4)) was adopted from Matoy et al. [39]:

$$f\left({}^{a}/_{w}\right) = 1.46 + 24.36\left({}^{a}/_{W}\right) - 47.21\left({}^{a}/_{w}\right)^2 + 75.18\left({}^{a}/_{w}\right)^3. \tag{4}$$

At each unloading cycle i, the crack extension (W-a_i) was calculated from the unloading stiffness and used to determine the crack initiation and crack propagation resistance.

$$W - a_i = \sqrt[3]{\frac{4 * k * L^3}{B * E}} \tag{5}$$

The plastic contribution $J_{plastic}$ to the J integral is obtained by

$$J^{(i)}_{plastic} = \int \frac{\eta\left(A_{Plastic\ local}\right)}{B(W-a_i)}, \tag{6}$$

where η is a constant ($\eta = 2$) and $A_{Plastic\ local}$ is the area under the load versus displacement curve. The J integral was calculated with its elastic and plastic contributions (Eq. (7)). Finally, J_Q was obtained based on

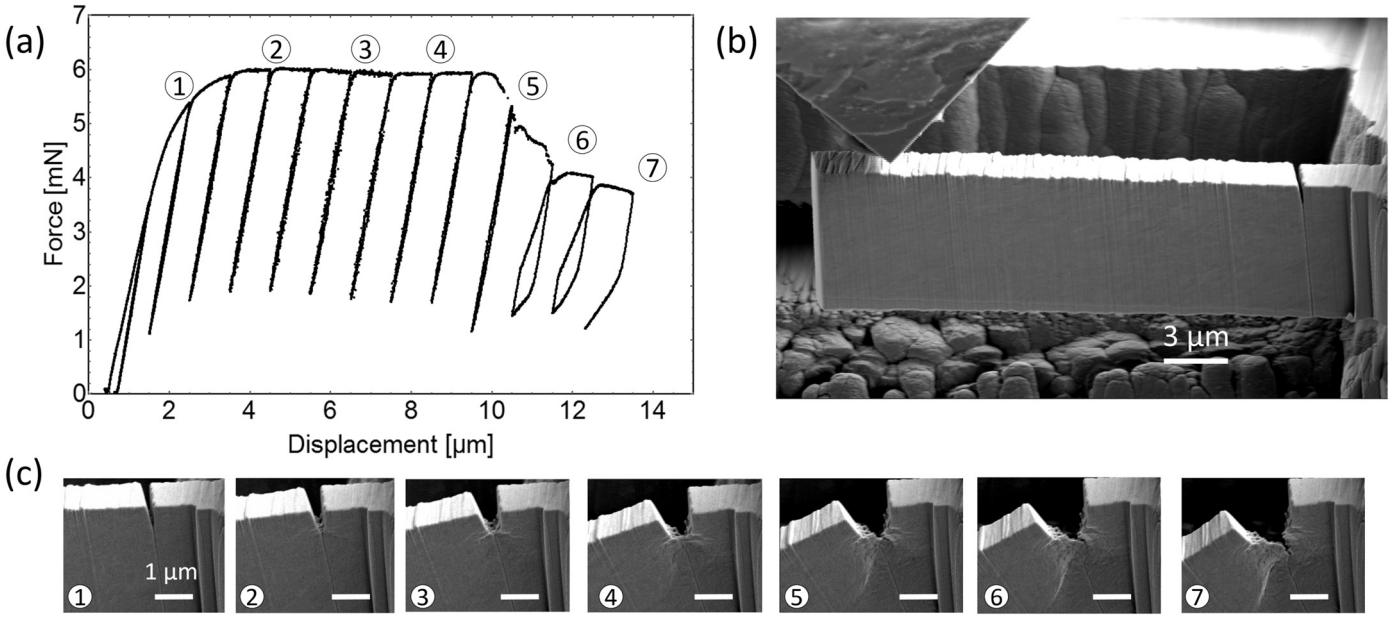

Fig. 3. (a) Representative force-displacement curve of a brown etching layer (BEL) sample. The curve shows the initial elastic and later significantly plastic deformation and fracture. (b) Secondary electron SEM image of the tested brown etching layer micro cantilever. (c) Sequential elasto-plastic crack propagation recorded by *in situ* SEM with positions highlighted in the force-displacement curve (a).

several criteria discussed in the results section. For comparison, J_Q was used to calculate K_Q Eq. (8).

$$J^{(i)} = \left(K_{IQ}^{(i)}\right)^2 \frac{(1-\nu^2)}{E} + \frac{2 * A_{Pl(i)}}{B * (w-a_0)} \tag{7}$$

$$K_{IQ} = \sqrt{J_{IQ} \frac{E}{(1-\nu^2)}} \tag{8}$$

3. Results

Cantilever fracture experiments exhibit stable crack propagation in the WEL. A representative force-displacement curve is shown in the Fig. 2a. After a linear initial loading regime plastic deformation sets in. Multiple partial unloading segments with a uniform interval of 1 μm are used to measure the change in cantilever stiffness. Subsequently, the stiffness change is used to calculate the crack propagation assuming a constant elastic modulus. A comparable force-displacement curve is observed for the lab simulated martensite. In contrast, the BEL samples and the undefomed pearlitic steel show slight differences in terms of a lack in force-reduction during crack propagation (see. Fig. 3a).

The stable crack propagation is in all cases reflected by the SEM images taken *in situ* at the indicated positions in the force-displacement curve (see Figs. 2c and 3c). The cracks are propagating in a straight direction and do not deflect from the intended crack plane. At the crack tip, significant plastic deformation is seen documenting the importance of plasticity to the energy dissipation during fracture. As expected, the undeformed pearlite shows the largest plastic contributions, which hinders the quantitative analysis of the fracture properties for that material. Hence, for undeformed pearlite we only provide a lower bound of the fracture toughness.

The stiffness for each unloading segment is calculated (Fig. 4a) and shows a decrease with displacement. Hence, the crack extension as calculated from Eq. (5) increases (Fig. 4b). The crack length of all considered samples estimated from stiffness measurement before and after bending experiment matches well with crack length measured from SEM. This

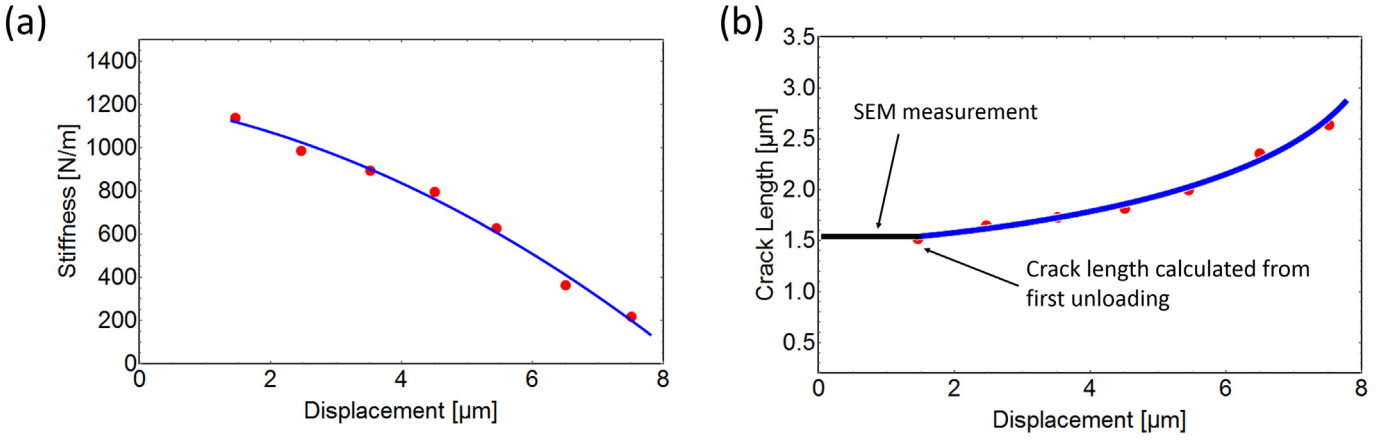

Fig. 4. (a) Stiffness of the loaded cantilever vs. indenter displacement. The stiffness was obtained from the unloading segments in the load displacement curves (Fig. 2a). The blue line is a polynomial fit to the data. (b) Corresponding increase in crack length as calculated from Eq. (5).

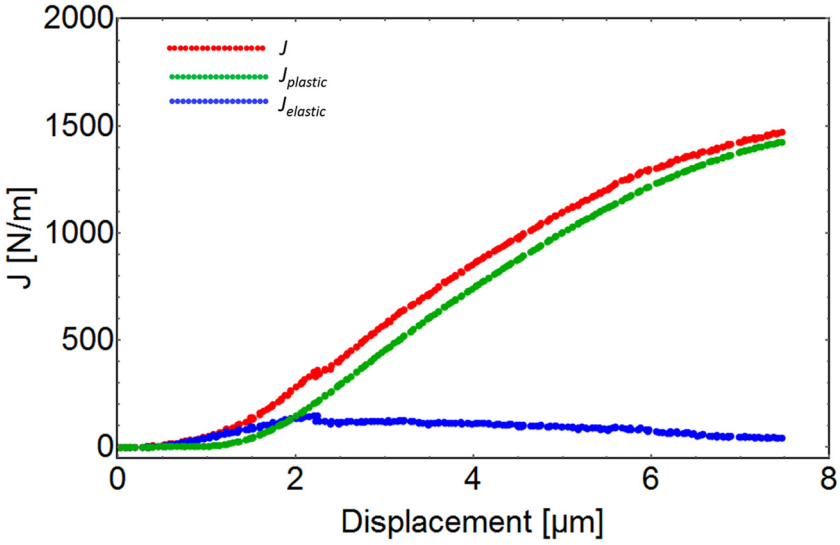

Fig. 5. The *J* integral (red) and the elastic (blue) and plastic (red) contributions to it for a WEL sample.

agreement is – for instance – observed in Fig. 4b, where the initial crack length is 1.5 μm as measured by SEM and as obtained from the first unloading stiffness (red point). It should be noted that some samples exhibit a stiffness increase which could be interpreted as crack closure, which is not the case. The reason for the apparent stiffness increase is addressed later. Specimens showing this phenomenon were not considered for the calculation of the mean fracture toughness.

As shown in Fig. 5, the *J* is quantified by addition of the elastic ($J_{elastic}$) and plastic ($J_{plastic}$) contribution part, see Eq. (7). During the initial loading segment, the elastic *J*-integral dominates. As soon as plastic deformation starts at the crack tip, $J_{plastic}$ dominates the *J* integral.

We further interpret the fracture behavior by plotting the *J* vs. Δa curve (crack resistance curve, Fig. 6). The crack resistance curve consists of the blunting line (first initial slope), where the artificial FIB milled notch starts to become a natural crack. Subsequently, stable crack growth becomes dominant. To quantitatively compare our crack resistance curve we use four previously published criteria:

(i) Pippan's transfer of ASTM standards to the microscale [40]
J_Q is standardized in ASTM E1820 for macro samples. The crack extension curve is fitted by a power law in a crack extension regime from 0.15 mm to 1.5 mm. The blunting line is defined by the slope of the power law at zero crack extension. Subsequently, J_0 (or $J_{0.2}$) are defined as the intersection of the crack extension curve with the blunting line that was shifted by 0.2 mm. Since FIB milled micro samples dissatisfy the geometrical requirements of the ASTM standards, Pippan et al. suggested using either 2% crack extension or 2% of the sample width instead of the 0.2 mm threshold [40]. To keep the spirit of ASTM standards, we fitted the power law in the crack extension range from $\Delta a =$ 1.5% to 15% and shifted the blunting line by an offset of $\Delta a =$ $0.02W$ (*W* is the initial sample thickness) to determine J_Q [40,41].

(ii) Wurster et al.'s approach based on the blunting line [31]
In Wurster's first criterion J_Q is the intersection of the blunting line with the fitted line of the stable crack growth regime, i.e. the crack resistance curve [31].

(iii) Wurster et al.'s [31] and Ast et al.'s [42] approach based on crack extension
In Wuster's second criterion, the *J* integral at a crack extension of 0.5 μm defines the J_Q. In their study, crack blunting was finished and stable crack growth was observed at this crack extension. Ast and co-workers observed negligible crack blunting and an immediate stable crack growth, therefore used a crack extension of $\Delta a = 0.2$ μm.

The *J*-integral values were analyzed for WEL, BEL, undeformed pearlite and lab simulated martensite using the four aforementioned criteria, as summarized in Table 1 and with a statistical analysis in Table 2. Nevertheless, the quantitative discussion of the material properties is based on Pippan's criterion only as this follows the ASTM spirits most closely.

The tested WELs always exhibit the smallest fracture toughness, which is on average 16.0 ± 1.2 MPa $m^{1/2}$.[1] In comparison, the lab simulated martensite is insignificantly tougher (17.4 ± 0.9 MPa $m^{1/2}$). Both, the BELs and the undeformed pearlite exhibit a significantly higher fracture toughness as the WELs. Besides the strong variation between the different regions (WELs, BELs, lab simulated martensite and undeformed pearlite), the toughness also varies within one region. For instance, the results of the three valid WEL micro samples are: 16.9 ± 2.6 MPa $m^{1/2}$, 13.5 ± 2.2 MPa $m^{1/2}$, 17.5 ± 2.6 MPa $m^{1/2}$. The variation in local toughness within one region is addressed to the local microstructure, i.e. the presence of grain boundaries, retained austenite, different orientations and etcetera [43]. Also, the used criteria strongly impacts the J_Q integral, irrespective of the tested material. The impact of the used criterion is discussed in the subsequent section.

4. Discussion

4.1. Reasons for the low fracture toughness of WEL compared to BEL

The fracture toughness of WELs is the lowest among all tested material systems indicating that WELs can be as brittle as a fully martensitic microstructure. The low fracture toughness of WELs is likely caused by the local microstructure consisting of ultrafine grains, which were formed by the combined effect of severe plastic deformation [44,45] and temperature. The WEL microstructure contains a high dislocation density [15] and carbon supersaturation [44]. Despite the grain size difference, this argumentation is supported by the comparable fracture toughness of the WEL and the lab simulated martensite with presumably similar carbon supersaturation.

[1] For quantitative comparisons we discuss only the toughness as evaluated by Pippan's transfer.

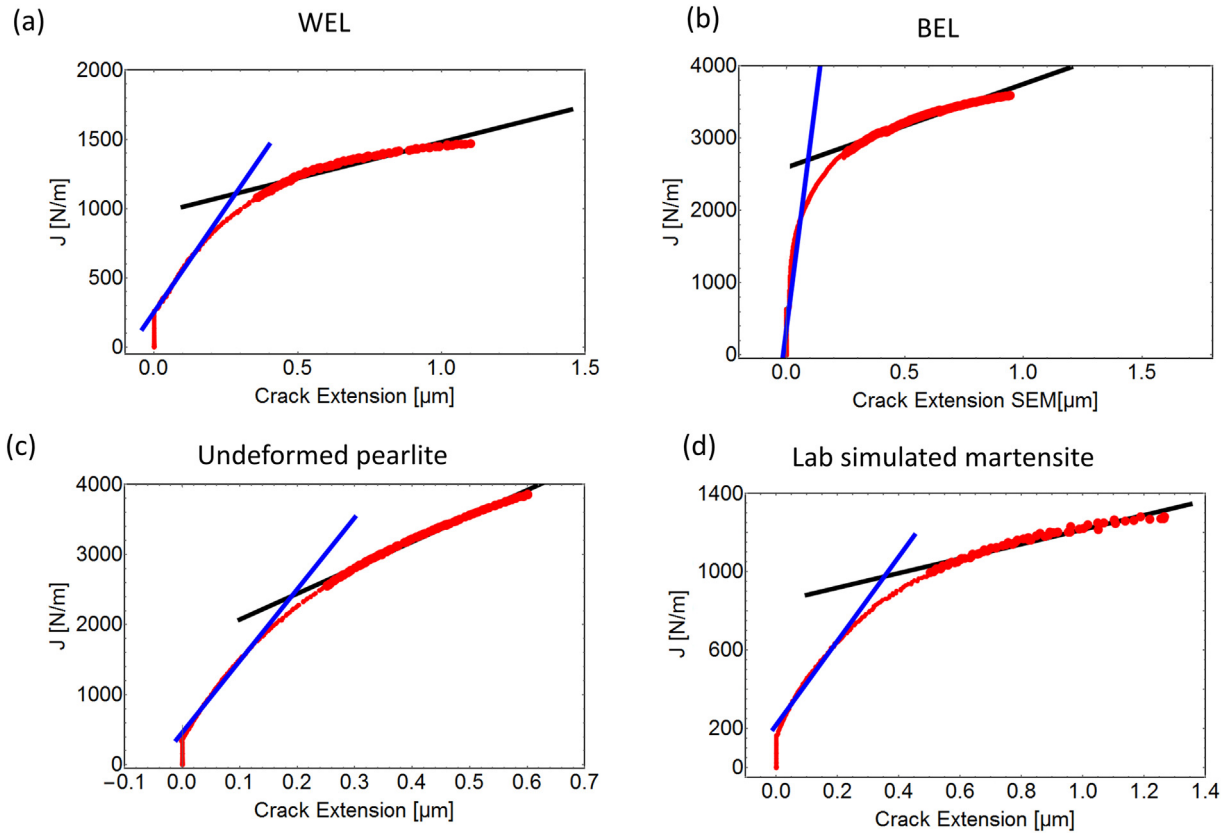

Fig. 6. Representative *J*-integral vs. crack extension graphs for WEL, BEL, undeformed pearlite and Lab simulated martensite. The blue curve indicates the blunting line. The black line is a fit to the stable crack growth of the natural crack.

The BEL is an intermediate microstructure between the WEL and the undeformed pearlite base material. Relatively to the WEL, the BEL has a higher fracture toughness and also shows significant crack tip plasticity. We attribute the higher fracture toughness to the lack of carbon supersaturation [38]. Due to the significant plasticity in the undeformed pearlite, a toughness comparison with the BEL is out of reach of this study. From the crack morphology, it can be concluded that the undeformed pearlite exhibits a significantly higher toughness than the BEL.

A common feature of structural materials is the inverse dependence of toughness and strength [46]. This relation holds true for the chemically identical microstructures formed during rolling contact fatigue from pearlitic steels. The higher the strength (hardness) the lower the fracture toughness (see Fig. 7). The data in Fig. 7 is used to estimate the fracture toughness from the local microhardness:

$$K_Q = \frac{A}{HV^B}, \tag{9}$$

We use a fitted function with K_Q as the local fracture toughness (in MPa $m^{1/2}$), *HV* as the Vickers micro hardness and A and B as the fitting constants. The data in Fig. 7 is best represent by $A = 15{,}600$ MPa $m^{1/2}$

Table 1
K_Q of all 12 successfully tested samples using various toughness criteria. The error bars represent the statistical error propagation. Note that in the case of the undeformed pearlite only lower bound values are provided.

Sample	$K_{Q,Pippan}$ (MPa $m^{1/2}$)	$K_{Q,Wurster,\ Slope}$ (At Δa = Slope) (MPa $m^{1/2}$)	$K_{Q,Wurster,\ 0.5}$ (At Δa = 0.5 μm) (MPa $m^{1/2}$)	$K_{Q,Ast}$ (At Δa = 0.2 μm) (MPa $m^{1/2}$)
WEL 1	16.9 ± 2.6	14.2 ± 2.2	16.6 ± 2.5	13.5 ± 2.0
WEL 2	13.5 ± 2.2	12.2 ± 2.0	13.8 ± 2.3	11.0 ± 1.8
WEL 3	17.5 ± 2.6	13.2 ± 1.9	12.8 ± 1.9	9.43 ± 1.4
BEL 1	21.2 ± 3.1	23.1 ± 3.4	24.2 ± 3.5	20.7 ± 3.0
BEL 2	24.3 ± 3.6	21.1 ± 3.1	16.5 ± 2.4	10.8 ± 1.6
BEL 3	23.8 ± 3.6	22.4 ± 3.4	22.6 ± 3.4	19.0 ± 2.8
Undeformed pearlite 1	>28	>23	>28	>22
Undeformed pearlite 2	>19	>16	>16	>13
Undeformed pearlite 3	>19	>13	>14	>10
Lab simulated 1	17.6 ± 2.7	15.9 ± 2.1	18.9 ± 2.9	13.6 ± 2.5
Lab simulated 2	15.8 ± 2.6	14.8 ± 2.4	14.9 ± 2.5	12.1 ± 2.0
Lab simulated 3	18.9 ± 2.7	11.7 ± 1.7	16.8 ± 2.4	15.1 ± 2.2

Table 2
Summary of K_Q for all materials. The error bars are given as the standard error of the mean.

Material	$K_{Q,Pippan}$ (MPa $m^{1/2}$)	$K_{Q,Wurster,\ Slope}$ (At Δa = Slope) (MPa $m^{1/2}$)	$K_{Q,Wurster,\ 0.5}$ (At $\Delta a = 0.5$ μm) (MPa $m^{1/2}$)	$K_{Q,Ast}$ (At $\Delta a = 0.2$ μm) (MPa $m^{1/2}$)	Number of valid samples
WEL	16.0 ± 1.2	13.2 ± 0.6	14.4 ± 1.1	11.3 ± 1.2	3/4
BEL	23.1 ± 1.0	22.2 ± 0.6	21.1 ± 2.4	17.0 ± 3.1	3/4
Undeformed pearlite	>28	>23	>28	>22	0/4
Lab simulated martensite	17.4 ± 0.9	15.3 ± 0.3	16.9 ± 1.2	12.5 ± 0.6	3/5

and $B = 1.0 \pm 0.3$, which describes all presented data with a relative error of <15% (except the undeformed pearlite samples of this study, which are not included in the fit). We propose to use $K_Q = 10^4/HV$ (K_Q in MPa $m^{1/2}$) as a more conservative estimate for the fracture toughness, which underestimates the obtained fracture toughness by up to 35% and therefore represents a higher safety factor. Please note that the Vickers hardness is specified in HV and not in MPa here.

4.2. Consequences of the low WEL fracture toughness

Based on the obtained fracture toughness and reported hardness, the critical defect size $a_{critical}$, at which a crack under the assumed stress state propagates, is estimated using Eq. (10),

$$K_Q = Y\sqrt{\pi\, a_{critical}}\,\sigma_y = Y\sqrt{\pi\, a_{critical}}\,\frac{H}{3}, \tag{10}$$

where Y is a dimensionless geometry factor of the order of 1, σ_y is the yield stress of the hypothetically maximum flow-stress determined from the hardness H via Tabor's relation. While a critical crack length in the order of 400 μm is determined for the macroscopic strength and toughness of rails (σ_y = 800–900 MPa, K_Q = 35–45 MPa $m^{1/2}$ [47]), the WEL has a significantly shorter critical crack length: the critical crack length $a_{critical}$ is on the order of 5–10 μm when using a Vickers hardness (~900 HV, [10,17,44,45]). This defect size is significantly smaller than the typical WEL thickness, which is typically 50–100 μm [15,17,18,44]. Single detached grain boundaries are excluded as crack nucleation sites, since the critical defect size is significantly larger than the grain size in WELs [13]. Hence, surface defects and non-metallic inclusions most likely act as crack initiation sites. These observations are in line with fractography of Carroll et al. [18] and Al-Juboori et al. [12].

In contrast, the critical crack length is larger than >50 μm in BEL due to the lower strength and higher fracture toughness. The larger critical crack length in BEL implies that crack nucleation occurs more likely in the WEL than the BEL.

4.3. Reasons for experimental data scatter

Throughout the study, we notice an increased experimental scatter compared to e.g. hard coatings [48]. Hence, the data scatter is not originating from the experimental methodology but rather from different local microstructures [12,17,38,43,44]. Therefore, the scatter represents the mechanical property distribution across the non-uniform microstructure rather than an experimental scatter caused by measurement inaccuracies. Furthermore, the fracture toughness of lab simulated martensite exhibits the narrowest distribution, which is caused by the uniform microstructure across the lab simulated martensite. For WELs, the wide distribution indicates that the fracture toughness will – in general – be position and history dependent, an observation which requires further in-depth investigations.

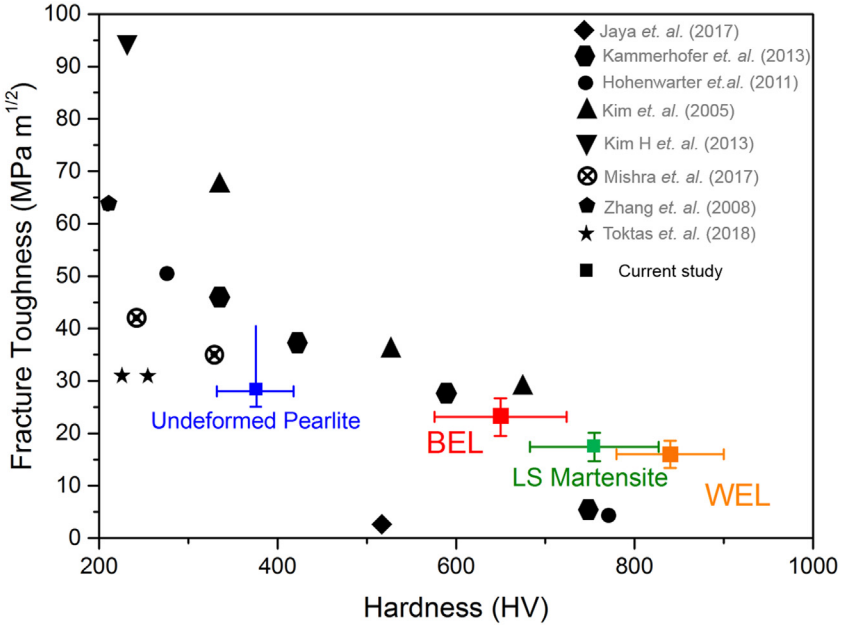

Fig. 7. Fracture toughness of all materials as a function of their corresponding Vickers hardness. The toughness of the WEL is similar to that of the lab simulated (LS) martensite. The toughness is inverse to the Vickers hardness. The fracture toughness is also compared to previous studies as marked in the graph [37,51–57].

In addition, the plastic deformation during WEL formation could result in a local variation of the residual stresses with unknown impact on the measured fracture toughness.

4.4. Effect of used toughness criteria

Until today, no accepted standards exist for downscaling elasto plastic fracture tests from the ASTM standards to the micron scale. Hence, we have applied and compared recently published criteria to analyze the toughness. Generally, the fracture toughness comparison is only valid if the same sample geometry and toughness criterion are used at the micron scale. Besides the sample dimensions, the crack geometry plays a significant role, as shown for LEFM [49,50]. For instance, bridge notch cantilevers of a WEL with slightly different microstructure show a different apparent fracture toughness [43]. However, applying the same geometry and toughness criterion allows for a relative comparison of the toughness.

Pippan's transfer criterion follows the spirit of the ASTM standards and is best suited to compare the fracture toughnesses of slightly differently sized samples. The intersection of the linear blunting line fit with the stable crack growth line allow for a certain change in sample size. By contrast, a fixed critical crack extension ($\Delta a = 0.2$ μm and $\Delta a = 0.5$ μm) does not allow for general toughness comparisons across sample sizes. The largest scatter was observed for the critical crack extension based criteria (e.g. $\Delta a = 0.2$ μm) even when using nominally identical cantilevers.

As already mentioned by Ast et al. [35], the Wurster intersection method and, likely, Pippan's transfer method are sometimes not applicable due the crack resistance curve shape.

4.5. Reasons for the stiffness increase during crack propagation

In some cases, we have observed an increasing stiffness at low cantilever deformations. A stiffness increase can falsely be interpreted as crack closure or crack healing, which was – as monitored by *in situ* SEM images – not the case in this study. However, the increase in sample stiffness originates from a small angular misalignment of the diamond wedge with respect to the cantilever surface. Due to the misalignment, an additional torque acts on the cantilever at low displacements. With increasing force, the misalignment is elastically compensated and the wedge aligns with the cantilever surface. This perfect alignment results in the maximum stiffness. Hence, until the point of parallel contact, an stiffness increase is observed, which must not be interpreted as crack closure / healing. After surpassing this point of parallel contact, any further crack growth reduces the sample stiffness. To avoid artefacts, we have omitted all experiments with an apparent crack closure at low loads.

It should be noted that in complex microstructures, such as martensitic steels, other effects might lead to a sample stiffness change and to substantial errors in the obtained crack extension curve. One such example is the transformation of initially metastable phases, e.g. retained austenite in steels.

5. Conclusions

Within this work we compare the fracture toughness of different regions in a rail-wheel contact by micron sized, elasto-plastic fracture experiments.

1) The toughness of microstructures with similar global chemical composition in a wheel-rail contact strictly follow the inverse toughness vs. hardness relation [46]. We propose to use the relation $J_Q = 10^4/HV$ (J_Q in MPa m$^{1/2}$) as predictive function for the local fracture toughness based on the local Vickers hardness. The prediction function is conservative and underestimates the fracture toughness by up to 35%.
2) WELs are considerable harder and, therefore, more prone to brittle failure than the undeformed pearlite and BEL. We obtained a toughness of 16 ± 1.2 MPa m$^{1/2}$ with Pippan's transfer criterion. This toughness is comparable to that of lab simulated martensite of the same chemical composition.
3) The critical defect size in WEL is estimated as 5–10 μm. Crack nucleation sites are therefore either non-metallic inclusions or surface damage. Cracks very likely do not originate from grain boundary decohesion in the nanostructured microstructure since the grain size is significantly smaller than the critical crack length.
4) BEL and pearlite are considerably tougher than WEL and it is expected that cracks initiate in the WEL only.
5) Different EPFM criteria result in largely different apparent fracture toughnesses. An absolute comparison of the toughnesses obtained from samples with varying geometry or from using different criteria is prone to substantial errors.

Data availability statement

The raw data obtained in this work can be made available upon request.

CRediT authorship contribution statement

Ashish Kumar Saxena: Data curation, Formal analysis, Writing - original draft. **Ankit Kumar:** Data curation. **Michael Herbig:** Writing - review & editing, Funding acquisition. **Steffen Brinckmann:** Methodology, Writing - review & editing. **Gerhard Dehm:** Writing - review & editing, Supervision. **Christoph Kirchlechner:** Methodology, Supervision, Writing - review & editing, Software.

Acknowledgement

We acknowledge Dr. Ivan Shevstov and Mr. Ruud from ProRail, the Netherlands, for keeping history and providing rail samples for this research and Dr. Jun Wu for providing the lab simulated martensite specimens. M. Herbig acknowledges funding by the German Federal Ministry of Education and Research (BMBF) through grant 03SF0535.

References

[1] A. Greco, S. Sheng, J. Keller, A. Erdemir, Material wear and fatigue in wind turbine systems, Wear 302 (2013) 1583–1591, https://doi.org/10.1016/j.wear.2013.01.060.
[2] M.-H. Evans, White structure flaking (WSF) in wind turbine gearbox bearings: effects of 'butterflies' and white etching cracks (WECs), Mater. Sci. Technol. 28 (2012) 3–22, https://doi.org/10.1179/026708311X13135950699254.
[3] Y.J. Li, M. Herbig, S. Goto, D. Raabe, Formation of nanosized grain structure in martensitic 100Cr6 bearing steels upon rolling contact loading studied by atom probe tomography, Mater. Sci. Technol. (United Kingdom). 32 (2016) 1100–1105, https://doi.org/10.1080/02670836.2015.1120458.
[4] H. Harada, T. Mikami, M. Shibata, D. Sokai, A. Yamamoto, H. Tsubakino, Microstructrural changes and crack initiation with white etching area formation under rolling/sliding contact in bearing steel, ISIJ Int. 45 (2005) 1897–1902.
[5] V. Šmeļova, A. Schwedt, L. Wang, W. Holweger, J. Mayer, Microstructural changes in White Etching Cracks (WECs) and their relationship with those in Dark Etching Region (DER) and White Etching Bands (WEBs) due to Rolling Contact Fatigue (RCF), Int. J. Fatigue 100 (2017) 148–158, https://doi.org/10.1016/j.ijfatigue.2017.03.027.
[6] A.V. Olver, The mechanism of rolling contact fatigue: an update, Proc. Inst. Mech. Eng. Part J J. Eng. Tribol. 219 (2005) 313–330, https://doi.org/10.1243/135065005X9808.
[7] S.B. Hosseini, M. Thuvander, U. Klement, G. Sundell, K. Ryttberg, Atomic-scale investigation of carbon atom migration in surface induced white layers in high-carbon medium chromium (AISI 52100) bearing steel, Acta Mater. 130 (2017) 155–163, https://doi.org/10.1016/j.actamat.2017.03.030.
[8] T.S. Eyre, A. Baxter, The formation of white layers at rubbing surfaces, Tribology 5 (1972) 256–261, https://doi.org/10.1016/0041-2678(72)90104-2.
[9] S.B. Newcomb, W.M. Stobbs, A transmission electron microscopy study of the white-etching layer on a rail head, Mater. Sci. Eng. 66 (1984) 195–204, https://doi.org/10.1016/0025-5416(84)90180-0.
[10] G. Baumann, H.J. Fecht, S. Liebelt, Formation of white-etching layers on rail treads, Wear 191 (1996) 133–140, https://doi.org/10.1016/0043-1648(95)06733-7.
[11] C. Bernsteiner, G. Müller, A. Meierhofer, K. Six, D. Künstner, P. Dietmaier, Development of white etching layers on rails: simulations and experiments, Wear. 366–367 (2016) 116–122, https://doi.org/10.1016/j.wear.2016.03.028.

[12] A. Al-Juboori, D. Wexler, H. Li, H. Zhu, C. Lu, A. McCusker, J. McLeod, S. Pannil, Z. Wang, Squat formation and the occurrence of two distinct classes of white etching layer on the surface of rail steel, Int. J. Fatigue 104 (2017) 52–60, https://doi.org/10.1016/j.ijfatigue.2017.07.005.

[13] W. Lojkowski, M. Djahanbakhsh, G. Bürkle, S. Gierlotka, W. Zielinski, H.J. Fecht, Nanostructure formation on the surface of railway tracks, Mater. Sci. Eng. A 303 (2001) 197–208, https://doi.org/10.1016/S0921-5093(00)01947-X.

[14] L. Wang, A. Pyzalla, W. Stadlbauer, E.A. Werner, Microstructure features on rolling surfaces of railway rails subjected to heavy loading, Mater. Sci. Eng. A 359 (2003) 31–43, https://doi.org/10.1016/S0921-5093(03)00327-7.

[15] W. Österle, H. Rooch, A. Pyzalla, L. Wang, Investigation of white etching layers on rails by optical microscopy, electron microscopy, X-ray and synchrotron X-ray diffraction, Mater. Sci. Eng. A 303 (2001) 150–157, https://doi.org/10.1016/S0921-5093(00)01842-6.

[16] S.L. Grassie, Squats and squat-type defects in rails: the understanding to date, Proc. Inst. Mech. Eng. Part F J. Rail Rapid Transit. 226 (2012) 235–242, https://doi.org/10.1177/0954409711422189.

[17] J. Takahashi, K. Kawakami, M. Ueda, Atom probe tomography analysis of the white etching layer in a rail track surface, Acta Mater. 58 (2010) 3602–3612, https://doi.org/10.1016/j.actamat.2010.02.030.

[18] R.I. Carroll, J.H. Beynon, Rolling contact fatigue of white etching layer: part 1. Crack morphology, Wear 262 (2007) 1253–1266, https://doi.org/10.1016/j.wear.2007.01.003.

[19] A. Grabulov, R. Petrov, H.W. Zandbergen, EBSD investigation of the crack initiation and TEM/FIB analyses of the microstructural changes around the cracks formed under Rolling Contact Fatigue (RCF), Int. J. Fatigue 32 (2010) 576–583, https://doi.org/10.1016/j.ijfatigue.2009.07.002.

[20] R.I. Carroll, J.H. Beynon, Rolling contact fatigue of white etching layer. Part 2. Numerical results, Wear 262 (2007) 1267–1273, https://doi.org/10.1016/j.wear.2007.01.002.

[21] J. Seo, S. Kwon, H. Jun, D. Lee, Numerical stress analysis and rolling contact fatigue of White Etching Layer on rail steel, Int. J. Fatigue 33 (2011) 203–211, https://doi.org/10.1016/j.ijfatigue.2010.08.007.

[22] M.D. Uchic, P.A. Shade, D.M. Dimiduk, Plasticity of micrometer-scale single crystals in compression, Annu. Rev. Mater. Res. 39 (2009) 361–386, https://doi.org/10.1146/annurev-matsci-082908-145422.

[23] O. Kraft, P.A. Gruber, R. Mönig, D. Weygand, Plasticity in confined dimensions, Annu. Rev. Mater. Res. 40 (2010) 293–317, https://doi.org/10.1146/annurev-matsci-082908-145409.

[24] G. Dehm, B.N. Jaya, R. Raghavan, C. Kirchlechner, Overview on micro- and nanomechanical testing: new insights in interface plasticity and fracture at small length scales, Acta Mater. 142 (2017) 248–282, https://doi.org/10.1016/j.actamat.2017.06.019.

[25] D. Di Maio, S.G. Roberts, Measuring fracture toughness of coatings using focused-ion-beam-machined microbeams, J. Mater. Res. 20 (2005) 299–302, https://doi.org/10.1557/JMR.2005.0048.

[26] B.N. Jaya, C. Kirchlechner, G. Dehm, Can microscale fracture tests provide reliable fracture toughness values? A case study in silicon, J. Mater. Res. 30 (2015) 686–698, https://doi.org/10.1557/jmr.2015.2.

[27] V. Schnabel, B.N. Jaya, M. Köhler, D. Music, C. Kirchlechner, G. Dehm, D. Raabe, J.M. Schneider, Electronic hybridisation implications for the damage-tolerance of thin film metallic glasses, Sci. Rep. 6 (2016) 1–12, https://doi.org/10.1038/srep36556.

[28] J.P. Best, J. Zechner, I. Shorubalko, J.V. Oboňa, J. Wehrs, M. Morstein, J. Michler, A comparison of three different notching ions for small-scale fracture toughness measurement, Scr. Mater. 112 (2016) 71–74, https://doi.org/10.1016/j.scriptamat.2015.09.014.

[29] R. Hahn, M. Bartosik, R. Soler, C. Kirchlechner, G. Dehm, P.H. Mayrhofer, Superlattice effect for enhanced fracture toughness of hard coatings, Scr. Mater. 124 (2016) 67–70, https://doi.org/10.1016/j.scriptamat.2016.06.030.

[30] R. Daniel, M. Meindlhumer, W. Baumegger, J. Zalesak, B. Sartory, M. Burghammer, C. Mitterer, J. Keckes, Grain boundary design of thin films: using tilted brittle interfaces for multiple crack deflection toughening, Acta Mater. 122 (2017) 130–137, https://doi.org/10.1016/j.actamat.2016.09.027.

[31] S. Wurster, C. Motz, R. Pippan, Characterization of the fracture toughness of micro-sized tungsten single crystal notched specimens, Philos. Mag. 92 (2012) 1803–1825, https://doi.org/10.1080/14786435.2012.658449.

[32] J. Ast, M. Göken, K. Durst, Size-dependent fracture toughness of tungsten, Acta Mater. 138 (2017) 198–211, https://doi.org/10.1016/j.actamat.2017.07.030.

[33] J. Ast, M. N. Polyakov, G. Mohanty, J. Michler, X. Maeder, Interplay of stresses, plasticity at crack tips and small sample dimensions revealed by in-situ microcantilever tests in tungsten, Mater. Sci. Eng. A 710 (2018) 400–412, https://doi.org/10.1016/j.msea.2017.10.096.

[34] D.E.J. Armstrong, A.S.M.A. Haseeb, S.G. Roberts, A.J. Wilkinson, K. Bade, Nanoindentation and micro-mechanical fracture toughness of electrodeposited nanocrystalline Ni-W alloy films, Thin Solid Films 520 (2012) 4369–4372, https://doi.org/10.1016/j.tsf.2012.02.059.

[35] J. Ast, T. Przybilla, V. Maier, K. Durst, M. Göken, Microcantilever bending experiments in NiAl - evaluation, size effects, and crack tip plasticity, J. Mater. Res. 29 (2014) 2129–2140, https://doi.org/10.1557/jmr.2014.240.

[36] A. Hohenwarter, M.W. Kapp, B. Völker, O. Renk, R. Pippan, Strength and ductility of heavily deformed pearlitic microstructures, IOP Conf. Ser. Mater. Sci. Eng. 219 (2017)https://doi.org/10.1088/1757-899X/219/1/012003.

[37] B.N. Jaya, S. Goto, G. Richter, C. Kirchlechner, G. Dehm, Fracture behavior of nanostructured heavily cold drawn pearlitic steel wires before and after annealing, Mater. Sci. Eng. A 707 (2017) 164–171, https://doi.org/10.1016/j.msea.2017.09.010.

[38] A. Kumar, G. Agarwal, R. Petrov, S. Goto, J. Sietsma, M. Herbig, Microstructural evolution of white and brown etching layers in pearlitic rail steels, Acta Mater. 171 (2019) 48–64, https://doi.org/10.1016/j.actamat.2019.04.012.

[39] K. Matoy, H. Schönherr, T. Detzel, T. Schöberl, R. Pippan, C. Motz, G. Dehm, D. Di Maio, S.G. Roberts, Measuring fracture toughness of coatings using focused-ion-beam-machined microbeams, J. Mater. Res. 20 (2009) 247–256, https://doi.org/10.1016/j.tsf.2009.07.143.

[40] R. Pippan, S. Wurster, D. Kiener, Fracture mechanics of micro samples: fundamental considerations, Mater. Des. 159 (2018) 252–267, https://doi.org/10.1016/j.matdes.2018.09.004.

[41] D. Yin, C.J. Marvel, F.Y. Cui, R.P. Vinci, M.P. Harmer, Microstructure and fracture toughness of electrodeposited Ni-21 at.% W alloy thick films, Acta Mater. 143 (2018) 272–280, https://doi.org/10.1016/j.actamat.2017.10.001.

[42] J. Ast, B. Merle, K. Durst, M. Göken, Fracture toughness evaluation of NiAl single crystals by microcantilevers—a new continuous J-integral method, J. Mater. Res. 31 (2016) 3786–3794, https://doi.org/10.1557/jmr.2016.393.

[43] A. Kumar, A.K. Saxena, C. Kirchlechner, M. Herbig, S. Brinkmann, R.H. Petrova, J. Sietsma, *In situ* study on fracture behaviour of white etching layers formed on rails, Submitt. to Acta Mater. (n.d.).

[44] H.W. Zhang, S. Ohsaki, S. Mitao, M. Ohnuma, K. Hono, Microstructural investigation of white etching layer on pearlite steel rail, Mater. Sci. Eng. A 421 (2006) 191–199, https://doi.org/10.1016/j.msea.2006.01.033.

[45] J. Wu, R.H. Petrov, M. Naeimi, Z. Li, R. Dollevoet, J. Sietsma, Laboratory simulation of martensite formation of white etching layer in rail steel, Int. J. Fatigue 91 (2016) 11–20, https://doi.org/10.1016/j.ijfatigue.2016.05.016.

[46] R.O. Ritchie, The conflicts between strength and toughness, Nat. Mater. 10 (2011) 817–822, https://doi.org/10.1038/nmat3115.

[47] F. Yu, P.Y. Ben Jar, M.T. Hendry, C. Jar, K. Nishanth, Fracture toughness estimation for high-strength rail steels using indentation test, Eng. Fract. Mech. 204 (2018) 469–481, https://doi.org/10.1016/j.engfracmech.2018.10.030.

[48] R. Soler, S. Gleich, C. Kirchlechner, C. Scheu, J.M. Schneider, G. Dehm, Fracture toughness of Mo2BC thin films: intrinsic toughness versus system toughening, Mater. Des. 154 (2018) 20–27, https://doi.org/10.1016/j.matdes.2018.05.015.

[49] S. Brinckmann, C. Kirchlechner, G. Dehm, Stress intensity factor dependence on anisotropy and geometry during micro-fracture experiments, Scr. Mater. 127 (2017) 76–78, https://doi.org/10.1016/j.scriptamat.2016.08.027.

[50] S. Brinckmann, K. Matoy, C. Kirchlechner, G. Dehm, On the influence of microcantilever pre-crack geometries on the apparent fracture toughness of brittle materials, Acta Mater. 136 (2017) 281–287, https://doi.org/10.1016/j.actamat.2017.07.014.

[51] C. Kammerhofer, A. Hohenwarter, S. Scheriau, H.P. Brantner, R. Pippan, Influence of morphology and structural size on the fracture behavior of a nanostructured pearlitic steel, Mater. Sci. Eng. A 585 (2013) 190–196, https://doi.org/10.1016/j.msea.2013.07.032.

[52] A. Hohenwarter, A. Taylor, R. Stock, R. Pippan, Effect of large shear deformations on the fracture behavior of a fully pearlitic steel, Metall. Mater. Trans. A Phys. Metall. Mater. Sci. 42 (2011) 1609–1618, https://doi.org/10.1007/s11661-010-0541-7.

[53] C.K. Kim, J. Il Park, S. Lee, Y. Chan Kim, N.J. Kim, J. Seung Yang, Effects of alloying elements on microstructure, hardness, and fracture toughness of centrifugally cast high-speed steel rolls, Metall. Mater. Trans. A Phys. Metall. Mater. Sci. 36 A (2005) 87–97, https://doi.org/10.1007/s11661-005-0141-0.

[54] H. Kim, M. Kang, H.J. Jung, H.S. Kim, C.M. Bae, S. Lee, Mechanisms of toughness improvement in Charpy impact and fracture toughness tests of non-heat-treating cold-drawn steel bar, Mater. Sci. Eng. A 571 (2013) 38–48, https://doi.org/10.1016/j.msea.2013.02.011.

[55] K. Mishra, A. Singh, Effect of interlamellar spacing on fracture toughness of nanostructured pearlite, Mater. Sci. Eng. A 706 (2017) 22–26, https://doi.org/10.1016/j.msea.2017.08.115.

[56] M.R. Zhang, H.C. Gu, Fracture toughness of nanostructured railway wheels, Eng. Fract. Mech. 75 (2008) 5113–5121, https://doi.org/10.1016/j.engfracmech.2008.07.007.

[57] G. Toktaş, A. Toktaş, Estimating fracture toughness of various matrix structured ductile iron using circumferentially notched tensile bars, Eng. Fract. Mech. 194 (2018) 1–8, https://doi.org/10.1016/j.engfracmech.2018.02.032.